communications materials

ARTICLE

https://doi.org/10.1038/s43246-022-00320-9 OPEN

Theory of holey twistsonic media

María Rosendo López [1], Zhiwang Zhang [2✉], Daniel Torrent[3] & Johan Christensen [1,4✉]

Rotating two overlapping lattices relative to each other produces the well known moiré interference patterns and has surprisingly led to strongly correlated superconductivity in twisted bilayer graphene. This seminal effect that is associated with electrons occupying flat dispersion bands has stimulated a surge of activities in classical wave physics such as acoustics to explore equivalent scenarios. Here, we mimic twisted bilayer physics by employing a rigorous sound wave expansion technique to conduct band engineering in holey bilayer plates, i.e., twistsonic media. Our numerical findings show how one flexibly is able to design moiré sound interference characteristics that alone are controlled by the twist angle and the interlayer air separation. More specifically, our numerical approach provides a significant advantage in both computational speed and storage size in comparison with widely used commercial finite-element-method solvers. We foresee that our findings should stimulate further studies in terms of band engineering and exotic topological twisted phases.

[1] Department of Physics, Universidad Carlos III de Madrid, Leganés, Madrid, Spain. [2] Department of Physics, MOE Key Laboratory of Modern Acoustics, Collaborative Innovation Center of Advanced Microstructures, Nanjing University, Nanjing, China. [3] GROC, UJI, Institut de Noves Tecnologies de la Imatge (INIT), Universitat Jaume I., Castellón, Spain. [4] IMDEA Materials Institute, Getafe, Madrid, Spain. ✉email: zhangzhiwang@nju.edu.cn; johan.christensen@imdea.org

The moiré effect is possibly best known from the shimmering effect seen when two geometrically regular arrangements are superimposed as in the case of overlaid textiles, fabrics, parallel lines, etc. These rippled appearances seem particularly impressive at acute angles, at which the overlaid and seemingly competing fabrics stand out at large intervals, i.e., waves with noticeable moiré wavelength. In an apparent unrelated area comprising atomically thin materials such as graphene, silicene, borophene, etc., or their assembled van der Waals heterostructures, a twist among them has shown to give rise to unprecedented electronic properties. Specifically, rotating two overlapping graphene monolayers at a so-called magic angle, gives rise to the collapse of their Dirac cones into flat dispersion bands, which is associated to an array of intriguing properties, such as 2D magnetism, Mott-insulating phases and unconventional superconductivity[1–6].

Generally speaking, lately, artificial sonic and phononic lattices have been used widely to explore with acoustic and elastic waves exotic topological phases and properties, which are hard and sometimes even out of reach to demonstrate in electronic settings. An attractive motivation compared to their electronic counterparts is their easy fabrication and tunability, which often reveal novel and unexpected effects to lead to entirely differing analogous connection to the original physical context. Chern insulators, valley-Hall phases and higher-order topological insulators are a few of many arenas that have been conquered with classical wave acoustics[7–16]. Among the latest efforts, several groups have already demonstrated that structured and twisted bilayer plates indeed host striking sonic, vibrating and photonic similarities compared to twisted bilayer graphene physics[17–22].

In this paper, we employ a theoretical approach to study how the twist angle, the plate separation and thickness are the responsible actors to enable moiré acoustic dispersion engineering in twistsonic media. The so-called mode-matching technique (MMT) enables us to conduct an entirely semi-numerical study of acoustic waves interacting with this complex twisted structure, on a much faster and storage-efficient basis compared to commercially available finite-element-method solvers like COMSOL. Our findings showcase how the band flatness, the spectral location of the bandgaps and the moiré interference patterns can be studied efficiently, thus providing useful insight into this contemporary branch of physics.

Results and discussion

Theory. Here we present a numerical technique that allows one to obtain the band structure of the twistsonic medium that consists of two rigid plates of thickness h_1 and h_2 that are separated by a thin gap of thickness h_g, as shown in Fig. 1. Both plates are perforated by round holes that are periodically distributed in a unit cell of size a_0. The unit cell contains N holes of radius $R_{0\alpha}$ located at the positions $\mathbf{R}_\alpha^1$ and $\mathbf{R}_\alpha^2$ where $\alpha = 1, 2, \ldots, N$. We separate the twistsonic medium into five different regions: region I refers to the first plate onto which sound waves impinge, region II refers to the field inside the through-holes of the first plate, region III refers to the gap separating the plates, region IV refers to the field inside the holes of the second plate and in region V sound is able to emerge into free-space as shown in Fig. 1b.

This separation of regions is the backbone of our theoretical formalism that is based on the MMT, which comprises a modal expansion of the involved pressure and velocity fields in these zones[23,24]. We assume that the surrounding medium is air with mass density and speed of sound $\rho_{\text{air}} = 1.225\,\text{kg/m}^3$ and $c_{\text{air}} = 343\,\text{m/s}$, respectively, and that the plates are made of steel or brass, in which the perfect rigid body approximation is very accurate. Thus, if an incident pressure wave P^{in} of unitary

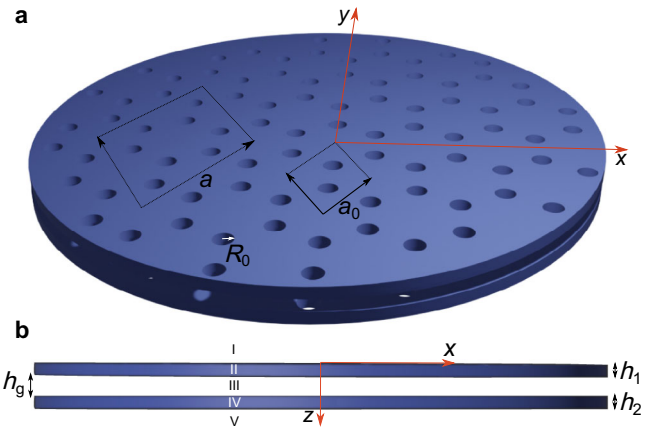

Fig. 1 The twistsonic medium. a The rigid bilayer is perforated with N round holes of radius R_0, which are arranged in a honeycomb lattice comprising a primitive unit cells of size a_0 and the moiré super cell of size a. **b** The side view of the structure enables one to distinguish the individual regions used for the MMT.

amplitude impinges the holey twistsonic medium, the wave will partially be reflected through diffracted sound and partially be funneled through the holey twistsonic medium. The pressure in regions I, III, and V is expanded in terms of plane waves whereas inside the α^{th} subwavelength hole (regions II and IV), only the fundamental cavity eigenmode is excited. The pressure fields in those regions read

$$\begin{aligned}
P_{\text{I}} &= \sum_{\mathbf{G}} Z_G\left(\delta_{\mathbf{G}0}e^{iq_{\mathbf{G}}z} + r_{\mathbf{G}}e^{-iq_{\mathbf{G}}z}\right)e^{i(\mathbf{K}+\mathbf{G})\cdot\mathbf{r}}\\
P_{\text{II}} &= Z\left(A_\alpha^{\text{II}}e^{iq_0 z} + B_\alpha^{\text{II}}e^{-iq_0 z}\right)\\
P_{\text{III}} &= \sum_{\mathbf{G}} Z_G\left(\tau_{\mathbf{G}}e^{iq_{\mathbf{G}}(z-\varphi_a)} + \Gamma_{\mathbf{G}}e^{-iq_{\mathbf{G}}(z-\varphi_a)}\right)e^{i(\mathbf{K}+\mathbf{G})\cdot\mathbf{r}}\\
P_{\text{IV}} &= Z\left(A_\alpha^{\text{IV}}e^{iq_0(z-\varphi_b)} + B_\alpha^{\text{IV}}e^{-iq_0(z-\varphi_b)}\right)\\
P_{\text{V}} &= \sum_{\mathbf{G}} Z_G t_{\mathbf{G}}e^{iq_{\mathbf{G}}(z-\varphi_c)}e^{i(\mathbf{K}+\mathbf{G})\cdot\mathbf{r}},
\end{aligned} \tag{1}$$

where $\mathbf{G}$ is the reciprocal lattice vector, $\mathbf{K}$ is the parallel wave vector, $k_0 = \omega/c_{\text{air}}$ is the free-space wavenumber, $\varphi_a = h_1$, $\varphi_b = h_1 + h_g$ and $\varphi_c = h_1 + h_g + h_2$ are out-of-plane phase contributions and $q_{\mathbf{G}} = \sqrt{k_0^2 - |\mathbf{K}+\mathbf{G}|^2}$. The radiation and hole impedances are written as $Z_G = k_0/q_{\mathbf{G}}$ and $Z = k_0/q_0$, respectively, whereas $r_{\mathbf{G}}$ ($t_{\mathbf{G}}$) is the reflection (transmission) coefficient and A_α, B_α are the modal cavity expansion coefficients. Likewise, continuity across the boundaries applies to the z-component, i.e., the normal component of the acoustic velocities that are

$$\begin{aligned}
v_z^{\text{I}} &= \sum_{\mathbf{G}}\left[\delta_{\mathbf{G}0}e^{iq_{\mathbf{G}}z} - r_{\mathbf{G}}e^{-iq_{\mathbf{G}}^{\text{I}}z}\right]e^{i(\mathbf{K}+\mathbf{G})\mathbf{r}}\\
v_z^{\text{II}} &= A_\alpha^{\text{II}}e^{iq_0 z} - B_\alpha^{\text{II}}e^{-iq_0 z}\\
v_z^{\text{III}} &= \sum_{\mathbf{G}}\left[\tau_{\mathbf{G}}e^{iq_{\mathbf{G}}(z-\varphi_a)} - \Gamma_{\mathbf{G}}e^{-iq_{\mathbf{G}}(z-\varphi_a)}\right]e^{i(\mathbf{K}+\mathbf{G})\mathbf{r}}\\
v_z^{\text{IV}} &= A_\alpha^{\text{IV}}e^{iq_0(z-\varphi_b)} - B_\alpha^{\text{IV}}e^{-iq_0(z-\varphi_b)}\\
v_z^{\text{V}} &= \sum_{\mathbf{G}} t_{\mathbf{G}}e^{iq_{\mathbf{G}}(z-\varphi_c)}e^{i(\mathbf{K}+\mathbf{G})\mathbf{r}}
\end{aligned} \tag{2}$$

As detailed in the Methods section, having all regional fields defined, we are now able to impose continuity of the respective fields across the respective interfaces. Moreover, the MMT is applied by projecting diffracted Bloch modes over the normal velocity fields and the fundamental cavity mode over the pressure field. This process introduces an in-plane phase contribution that defines the intra-layer hole-to-hole interaction within the moiré supercell. Additionally, at each interface site, we define a set of

modal velocities:

$$\begin{aligned} v_{1\alpha} &= A_\alpha^{\mathrm{II}} - B_\alpha^{\mathrm{II}} \\ v'_{1\alpha} &= -\left(A_\alpha^{\mathrm{II}} e^{iq_0h_1} - B_\alpha^{\mathrm{II}} e^{-iq_0h_1}\right) \\ v_{2\alpha} &= A_\alpha^{\mathrm{IV}} - B_\alpha^{\mathrm{IV}} \\ v'_{2\alpha} &= -\left(A_\alpha^{\mathrm{IV}} e^{iq_0h_2} - B_\alpha^{\mathrm{IV}} e^{-iq_0h_2}\right), \end{aligned} \tag{3}$$

which allow for a highly compact and insightful representation of the holey twistsonic medium,

$$\begin{aligned} &\left(G_1^{\alpha\alpha} - \epsilon_1\right)v_{1\alpha} + \sum_{\beta\neq\alpha} G_1^{\alpha\beta} v_{1\beta} - G_1^V v'_{1\alpha} = I^\alpha \\ &\left(\psi_{\alpha\alpha}^1 + \epsilon_1\right)v'_{1\alpha} + \sum_{\beta\neq\alpha} \psi_{\alpha\beta}^1 v'_{1\beta} + \sum_{\beta} \Phi_{\alpha\beta}^1 v_{2\beta} + G_1^V v_{1\alpha} = 0 \\ &\left(\psi_{\alpha\alpha}^2 + \epsilon_2\right)v_{2\alpha} + \sum_{\beta\neq\alpha} \psi_{\alpha\beta}^2 v_{2\beta} + \sum_{\beta} \Phi_{\alpha\beta}^2 v'_{1\beta} + G_2^V v'_{2\alpha} = 0 \\ &\left(G_2^{\alpha\alpha} - \epsilon_2\right)v'_{2\alpha} + \sum_{\beta\neq\alpha} G_2^{\alpha\beta} v'_{2\beta} - G_2^V v_{2\alpha} = 0 \end{aligned} \tag{4}$$

where:

$$\begin{aligned} I^\alpha &= \sum_{\mathbf{G}} 2Z_{\mathbf{G}}^I \delta_{\mathbf{G}0} H_\alpha^1(\mathbf{G}) \\ H_\alpha^{1(2)}(\mathbf{G}) &= \frac{2J_1(R_{0\alpha}|\mathbf{K}+\mathbf{G}|)}{R_{0\alpha}|\mathbf{K}+\mathbf{G}|} e^{i(\mathbf{K}+\mathbf{G})\mathbf{R}_\alpha^{1(2)}} \\ G_1^V &= \frac{Z^{II}}{i\sin(q_0h_1)} \quad G_2^V = \frac{Z^{II}}{i\sin(q_0h_2)} \\ \epsilon_1 &= \frac{Z^{II}}{i\tan(q_0h_1)} \quad \epsilon_2 = \frac{Z^{II}}{i\tan(q_0h_2)} \\ G_{\alpha\beta}^{1(2)} &= \sum_{\mathbf{G}} Z_{\mathbf{G}}^I H_\beta^{*1(2)}(\mathbf{G}) f_\beta H_\alpha^{1(2)}(\mathbf{G}) \\ \psi_{\alpha\beta}^{1(2)} &= \sum_{\mathbf{G}} \frac{Z_{\mathbf{G}}^I H_\beta^{*1(2)}(\mathbf{G}) f_\beta H_\alpha^{1(2)}(\mathbf{G})}{i\tan(q_{\mathbf{G}}^I h_g)} \\ \Phi_{\alpha\beta}^{1(2)} &= \sum_{\mathbf{G}} \frac{Z_{\mathbf{G}}^I H_\beta^{*1(2)}(\mathbf{G}) f_\beta H_\alpha^{1(2)}(\mathbf{G})}{i\sin(q_{\mathbf{G}}^I h_g)} \\ f_\beta &= \frac{\Omega_\beta}{\Omega} = \frac{\pi R_{0\beta}^2}{\sqrt{3}a^2/2}. \end{aligned} \tag{5}$$

The terms introduced in the system, all have a physical interpretation. I^α is the irradiation term over the fundamental cavity mode of the α^{th} hole of the first plate, $H_\alpha^{1(2)}$ is the overlap function, $\epsilon_{1(2)}$ is related to the acoustic bouncing back and forth inside the holes, $G_{1(2)}^V$ refers to the coupling of the two sides of each hole, $G_{\alpha\beta}^{1(2)}$ measures the coupling between the holes of each plate, and finally, $\psi_{\alpha\beta}^{1(2)}$ and $\Phi_{\alpha\beta}^{1(2)}$ account for coupling across the plates. Upon solving the unknown modal coefficients of Eq. (4), both the cavity expansion and the scattering coefficients can be determined. The latter can be specifically expressed as

$$\begin{aligned} r_{\mathbf{G}} &= \delta_{\mathbf{G}0} - \sum_\beta v_\beta H_\beta^*(\mathbf{G}) f_\beta \\ t_{\mathbf{G}} &= -\sum_\beta v'_\beta H_\beta^*(\mathbf{G}) f_\beta. \end{aligned} \tag{6}$$

Moreover, in the absence of incoming sound, i.e., $I^\alpha = 0$, computing the zero determinant of Eq. (4) as a function of both frequency and the parallel momentum, allows us to determine the dispersion relation in dependence of the geometrical parameters. More importantly though, also in dependence of the rotation angle of the holey twistsonic medium.

Numerical results. In numerically treating the holey twistsonic medium, the upper layer is considered perforated by N holes that are placed at sites $\mathbf{R}_\alpha^1 = n_1\mathbf{a}_1 + n_2\mathbf{a}_2$, forming a honeycomb lattice of period a_0 and lattice vectors $\mathbf{a}_{1,2} = a_0[\pm\cos(\pi/3), \sin(\pi/3)]$. Beyond this, the N holes of the bottom layer are placed at $\mathbf{R}_\alpha^2 = m_1\mathbf{b}_1 + m_2\mathbf{b}_2$ where the vectors $\mathbf{b}_{1,2}$ are the rotated counterparts to $\mathbf{a}_{1,2}$ to account for the twisting. All holes in the study have circular cross section of radius $R_{0\alpha} = 0.25a_0$. Note that the moiré pattern in twisted bilayer is not always commensurate with the original lattice period. Among all possible twisting angles we can work with, the commensurate angles $\theta = \arccos[(3m^2+3m+1/2)/(3m^2+3m+1)]$, for some integers m, are the ones defining the size of the resulting superlattice and its underlying sonic moiré interference pattern. Hence, the twisting induced moiré lattice constant becomes $L_m = a = a_0/\left[2\sin(\theta/2)\right]$, with its corresponding site parameters $\mathbf{R}_m = q_1\mathbf{t}_1 + q_2\mathbf{t}_2$, with $\mathbf{t}_{1,2} = L_m[\pm\cos(\pi/6), \sin(\pi/6)]$. In what follows, we show how the size of the supercell alters the dispersive nature of the holey twisted structure, however, additionally, we discuss how the gap separation and the plate thickness change the band flatness and its spectral location, respectively. In this study, we concentrate on twistsonic media comprising three twist angles, which means we have to construct three different superlattices. With respect to the above given formula, we fix those three configurations, as summarized in Table 1.

Table 1 Parameters of the superlattices of three holey twistsonic media under study.

Rotation angle θ	m	Number of holes N	Period a
21.78°	1	14	$2.65a_0$
13.17°	2	38	$4.36a_0$
9.43°	3	74	$6.08a_0$

Figure 2 displays multiple computed dispersion relations of twistsonic configurations with constant hole radius and plate thickness as captured in the figure. The three rows indicate computations at constant unit cell size, whereas the rows represent a successive shrinking of the gap separation, i.e., $h_g = 0.8a_0$, to $h_g = 0.5a_0$. The solutions of the system correspond to vanishing determinants, whereas the dispersionless soundlines, i.e., the lattice singularities are accompanied with large determinant values that are not solutions to the problem. Reducing the twist angle, i.e., increasing the superlattice size leads to an obvious change of the moiré interference pattern that is indicated by strong modifications of the dispersionless sound lines seen throughout all examples in Fig. 2. Moreover, at the K-points in the band diagrams, we predict distinctive Dirac cones whose respective touching points reside at identical frequencies (red circles). A more distinctive feature of the computations is the compression of these Dirac cones when the two involved plates are pushed together. E.g., for $m = 2$ at around $ka_0/2\pi = 0.215$ we see that the flatness of the dispersion bands of the cones appear more pronounced when h_g is steadily decreased. This finding shows that not only twisting towards the magic angle can lead to band flatness, but a more accessible approach, namely to tune the plate separation, can lead to an equivalent effect. In the following subsection, we further compare the MMT with the finite-element method and find that the MMT displays superior advantages, both in terms of the computational speed and the storage size.

In the same spirit with the foregoing study in Fig. 2, we now fix the gap separation as indicated in the caption of Fig. 3, but next to varying the twist angle ($m = 1$–3) we also increase the plate thicknesses, $h = h_1 = h_2$. What immediately stands out in all computed band diagrams for the chosen twist angles, is that an increase of the thickness of both plates leads to a redshift (towards lower frequencies) of the dispersion branches. We

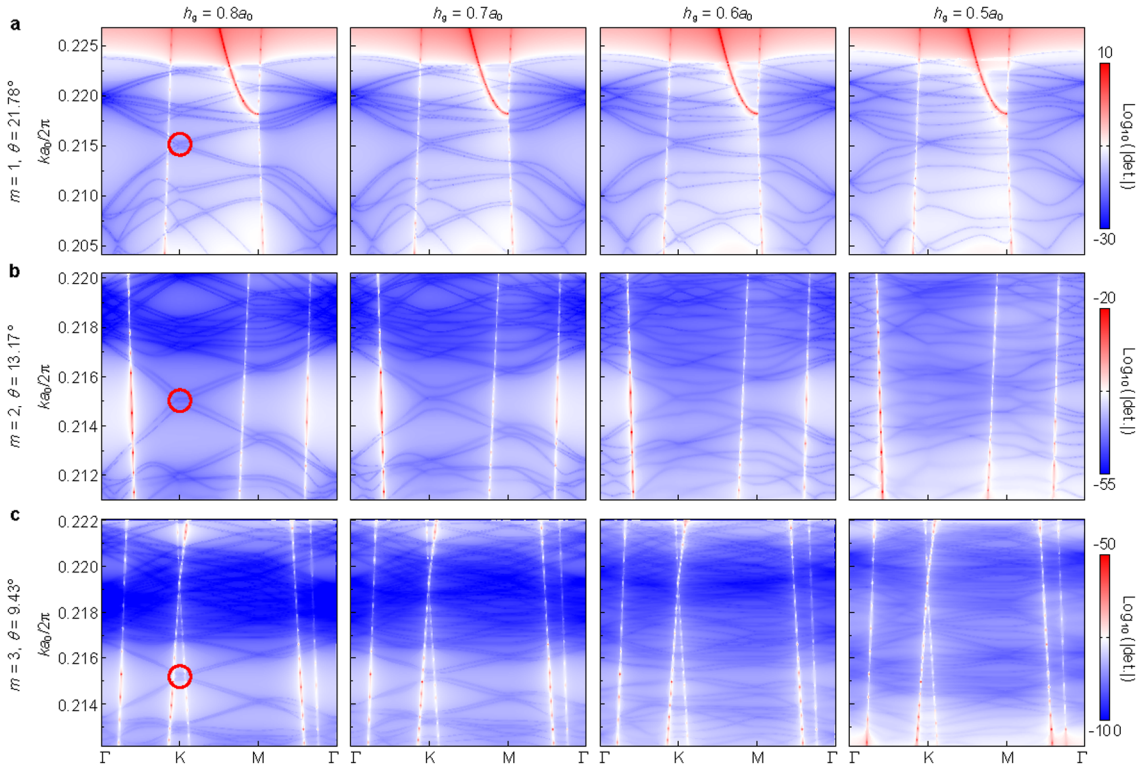

Fig. 2 Dispersion relation of the holey twistsonic medium with different gap separations h_g and twist angles. Specifically, we vary the gap from $h_g = 0.8a_0$ to $h_g = 0.5a_0$ (four columns) and twist the bilayer according to **a** $m = 1$ ($\theta = 21.78°$), **b** $m = 2$ ($\theta = 13.17°$), and **c** $m = 3$ ($\theta = 9.43°$). The plate thickness is fixed at $h_1 = h_2 = h = 2a_0$. Red circles mark the regions of the field plots in Fig. 4.

observe a complex interplay among moiré scattering features and localized Fabry-Perot type resonances. The latter originates from multiple λ-half (wavelength $\lambda = 2\pi/k_0$) resonances within the perforations[23]. Increasing the plate thickness as in the present study thus leads to holey twistsonic media capable to host Dirac features for longer wavelength, i.e., their redshift with growing plate thickness.

In order to visualize the acoustic moiré interference fringes, we compute the pressure fields at spectral regions marked by red circles in Fig. 2. We chose to inspect the insonified side of the holey twistsonic media, i.e., region I in Fig. 1, onto which sound waves impinge, thus the first pressure field in Eq. (1) is to be considered in connection with its complex reflection coefficient in Eq. (6). In doing so, we first solve the equations in Eq. (4) to obtain the modal fields. Afterwards, we calculate the reflection coefficient $r_{\mathbf{G}}$ in Eq. (6), upon which we introduce it in the expression of P_{I} in Eq. (1) for the chosen plane. At the nearest vicinity of the upper holey plate ($z = -0.001a_0$) of the three structures under study, the back-reflected sound unequivocally displays the fingerprints of the periodic moiré fringes as the computations in Fig. 4 showcase. We have taken a square-shaped domain ($10a_0 \times 10a_0$) in each case, to display the scattered moiré features for comparison. A remarkable attribute in using holey plates as artificial twisted structures can be discerned upon close inspection of the field plots, which is the said complex interplay between twisted induced moiré pattern and acoustic energy concentrated within the holes.

Comparing the MMT with the finite-element method. In this section, we discuss the advantages of the MMT after comparison with the widely used commercial finite-element-method solver COMSOL.

(i) The computational speed of the MMT is faster. We demonstrate that one of the advantages of the MMT is the computational speed. As shown in Fig. 5, the band diagrams of identical structures (see caption) are calculated with the MMT (implemented using the Julia Programming Language) and by using the commercial finite-element-method (FEM) simulation software COMSOL Multiphysics. The obtained bands show good agreement except for a negligible frequency shift. To compare the computational speed, along the wave vector axis both methods have identical intervals, i.e., 50 steps. Since the number of frequencies in COMSOL depends on the available number of eigensolution, in the MMT we chose 500 points. We ran the MMT and the FEM COMSOL computations one by one using the same computer, which is a Dell Precision 7920 workstation with a Intel(R) Xeon(R) Silver 4210 CPU and 640 GB of RAM. The computational time using COMSOL is 8077s, whereas that of the MMT is only 407s, which is almost 20 times faster.

(ii) The storage size of the MMT code is smaller. The storage size of the FEM COMSOL file is about 1.27×10^7 kB, while the storage size of the MMT code is only 416 kB, which is about 3.28×10^5 times smaller.

Conclusions

Holey twistsonic media, i.e., the acoustic counterpart of twisted bilayer graphene have been studied semi-numerically thanks to a modal expansion approach. In contrast to widely used commercial finite element solvers, our technique produces relatively fast dispersion relations results without sacrificing storage space. Holey plates are highly flexible and tunable structures for metamaterials, topological and twistsonic applications. Hence, we believe that our tool should serve as solid basis to conduct experimental studies along this line. We showed how these acoustic twisted media not only host these flat moiré dispersion

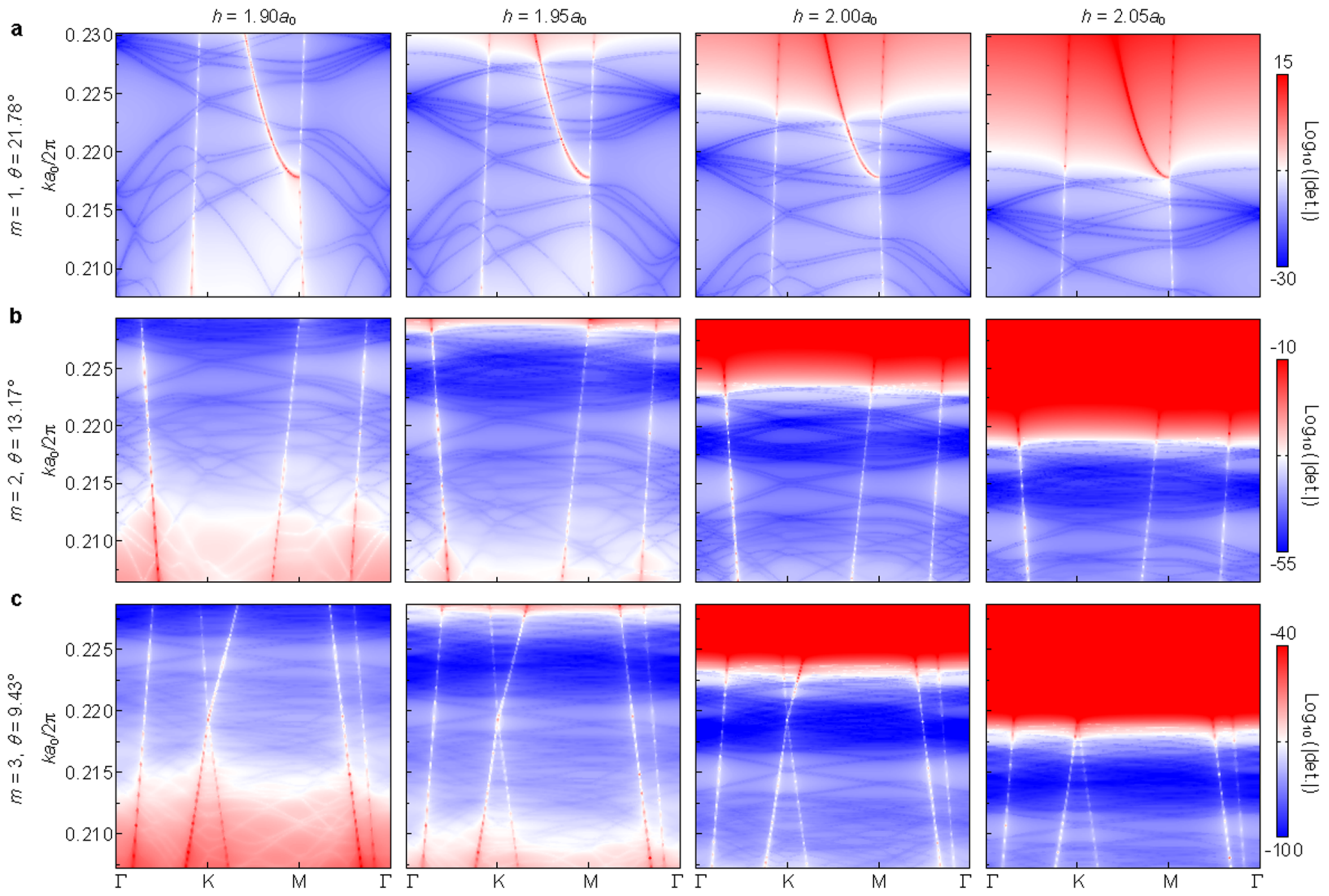

Fig. 3 Dispersion relation of the holey twistsonic medium with different plate thickness *h* and twist angles. We vary the plate thickness ($h = h_1 = h_2$) from $h = 1.90a_0$ to $h = 2.05a_0$ (four columns) and twist the bilayer according to **a** $m = 1$ ($\theta = 21.78°$), **b** $m = 2$ ($\theta = 13.17°$), and **c** $m = 3$ ($\theta = 9.43°$). The gap separation is fixed at $h_g = 0.8a_0$.

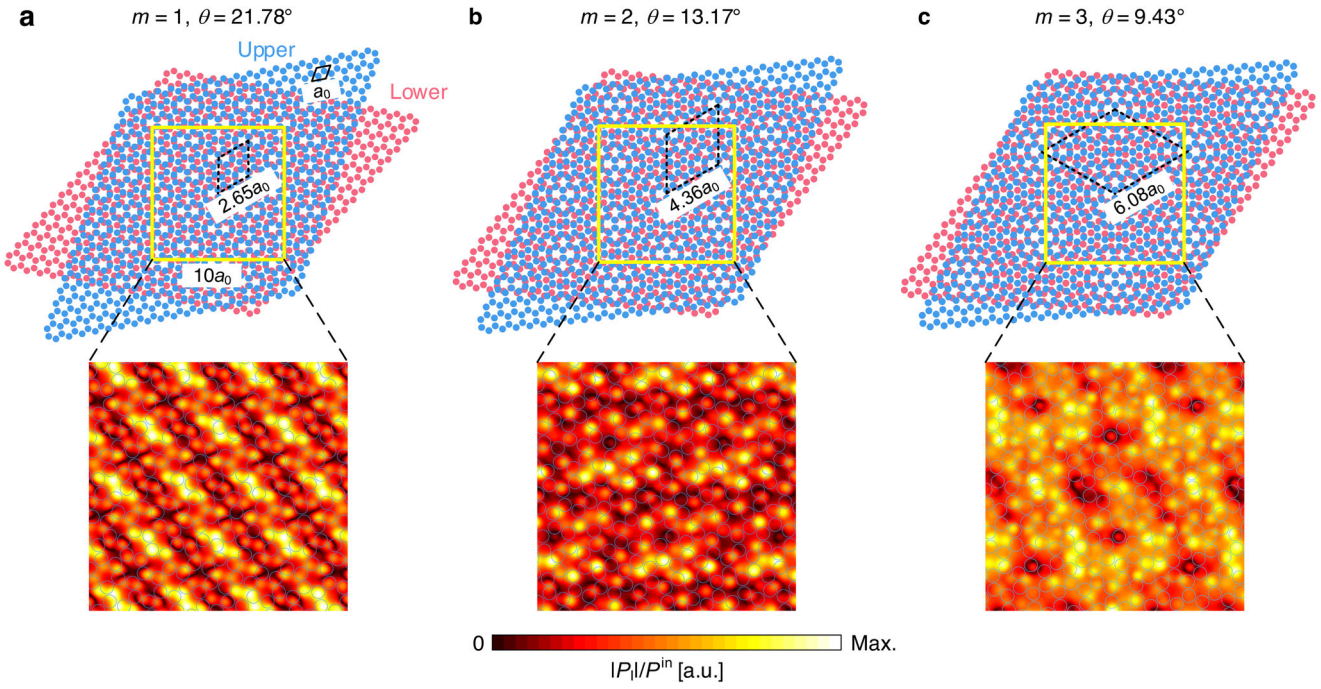

Fig. 4 Schematic and Moiré pressure fields at the Dirac cones for three different superlattices. The field plot regions correspond to the red circles in the band diagram of Fig. 2, with **a** $m = 1$, **b** $m = 2$, and **c** $m = 3$, respectively, and the geometrical parameters $h_g = 0.8a_0$ and $h_{1,2} = 2a_0$. At the plane $z = -0.001a_0$ we map the normalized pressured fields $|P_l|/P^{in}$. Here, the blue circles in the contour plots indicate the holes' positions on the upper plate.

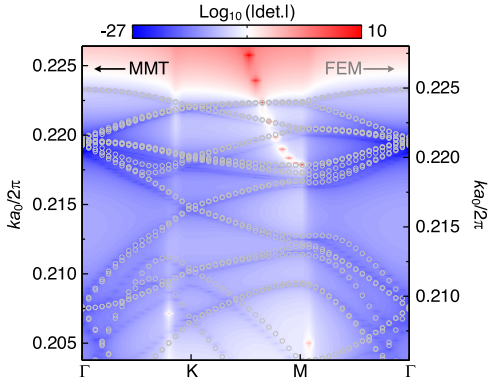

Fig. 5 Comparison between MMT and the FEM calculations. Band diagrams calculated with the MMT (blue lines) and the FEM (gray circles). The geometrical parameters are $m = 1$, $\theta = 21.78°$, $h = 2a_0$ and $h_g = 0.8a_0$.

bands, but moreover, that they can be straightforwardly altered through the involved geometry.

Methods

The semi-analytical method used to compute the dispersion relations as well as the pressure fields is the Mode Matching Technique, whose details are derived in this section.

Let us assume that we have two acoustically rigid plates of thickness h_1 and h_2 placed in the xy plane at $z = 0$. Both plates are periodically perforated by N round holes of radius $R_{0\alpha}$ and located at the positions $\mathbf{R}_\alpha^1$ and $\mathbf{R}_\alpha^2$ where $\alpha = 1, 2, \ldots, N$ in a unit cell of size a_0. These two plates are separated by a thin layer of thickness h_g. We assume that the plates are made of steel or brass, in which the perfect rigid body approximation is very accurate. If the system is irradiated by an incident wave P^{in} of unitary amplitude and propagating along the z axis with wavenumber $\mathbf{k} = \mathbf{K} + q_0\hat{\mathbf{z}}$, the same scattering properties are obtained in different frequency regimes by scaling all the geometrical parameteres with the same factor.

In order to apply the Mode Matching Technique, five different regions are taking into account: region I refers to the first plate onto which sound waves impinge, region II refers to the field inside the through-holes of the first plate, region III refers to the gap separating the plates, region IV refers to the field inside the holes of the second plate and in region V sound is able to emerge into free-space. We assume that the surrounding medium is air, with the mass density ρ_{air} and speed of sound c_{air}.

In regions I, III and V the pressure is expanded in terms of plane waves whereas inside the holes the field is written as a linear combination of the corresponding waveguide eigenmodes:

$$\begin{aligned}
P_{\text{I}} &= P^{in} + P_R = \sum_{\mathbf{G}} Z_G\left(\delta_{\mathbf{G}0}e^{iq_{\mathbf{G}}z} + r_{\mathbf{G}}e^{-iq_{\mathbf{G}}z}\right)e^{i(\mathbf{K}+\mathbf{G})\mathbf{r}}\\
P_{\text{II}} &= Z\left(A_\alpha^{II}e^{iq_0 z} + B_\alpha^{II}e^{-iq_0 z}\right)\\
P_{\text{III}} &= \sum_{\mathbf{G}} Z_G\left(\tau_{\mathbf{G}}e^{iq_{\mathbf{G}}(z-\varphi_a)} + \Gamma_{\mathbf{G}}e^{-iq_{\mathbf{G}}(z-\varphi_a)}\right)e^{i(\mathbf{K}+\mathbf{G})\mathbf{r}}\\
P_{\text{IV}} &= Z\left(A_\alpha^{IV}e^{iq_0(z-\varphi_b)} + B_\alpha^{IV}e^{-iq_0(z-\varphi_b)}\right)\\
P_{\text{V}} &= P_T = \sum_{\mathbf{G}} Z_G t_{\mathbf{G}}e^{iq_{\mathbf{G}}(z-\varphi_c)}e^{i(\mathbf{K}+\mathbf{G})\mathbf{r}}
\end{aligned} \tag{7}$$

where $\mathbf{G}$ is the reciprocal lattice vector, $\mathbf{K}$ is the Bloch wave vector, $k_0 = \omega/c_{air}$ is the incident wave vector, $\varphi_a = h_1$, $\varphi_b = h_1 + h_g$ and $\varphi_c = h_1 + h_g + h_2$ are the phases we introduce in order to center the axis in the bottom or upper part of the layers, $q_{\mathbf{G}} = \sqrt{k_0^2 - |\mathbf{K}+\mathbf{G}|^2}$. The radiated and hole impedance are written as $Z_G = k0/q_{\mathbf{G}}$ and $Z = k_0/q_0$, respectively, whereas $r_{\mathbf{G}}(t_{\mathbf{G}})$ is the reflection (transmission) coefficient and A_α, B_α are the modal cavity expansion coefficients. Based on the subwavelength scales of the holes, it is assumed that only their fundamental mode is exited, so $q_0 = c_1/c_2 k_0$.

In the following, we show the normal velocity within the different regions, which is obtained deriving the pressure of each region with respect to the z-axis.

$$\begin{aligned}
v_z^I &= \sum_{\mathbf{G}}\left[\delta_{\mathbf{G}0}e^{iq_{\mathbf{G}}z} - r_{\mathbf{G}}e^{-iq_{\mathbf{G}}z}\right]e^{i(\mathbf{K}+\mathbf{G})\mathbf{r}}\\
v_z^{II} &= A_\alpha^{II}e^{iq_0 z} - B_\alpha^{II}e^{-iq_0 z}\\
v_z^{III} &= \sum_{\mathbf{G}}\left[\tau_{\mathbf{G}}e^{iq_{\mathbf{G}}(z-\varphi_a)} - \Gamma_{\mathbf{G}}e^{-iq_{\mathbf{G}}(z-\varphi_a)}\right]e^{i(\mathbf{K}+\mathbf{G})\mathbf{r}}\\
v_z^{IV} &= A_\alpha^{IV}e^{iq_0(z-\varphi_b)} - B_\alpha^{IV}e^{-iq_0(z-\varphi_b)}\\
v_z^{V} &= \sum_{\mathbf{G}} t_{\mathbf{G}}e^{iq_{\mathbf{G}}(z-\varphi_c)}e^{i(\mathbf{K}+\mathbf{G})\mathbf{r}}
\end{aligned} \tag{8}$$

The Mode Matching Technique is applied by projecting the Bloch modes with the normal velocity field and the cavity modes for the pressure field:

- **Pressure**: First, we impose the continuity of the pressure at the upper ($z = 0$) and bottom ($z = h$) part of the α holes:

$$\begin{aligned}
\iint_{\Omega_\alpha} P_{\text{I}}|_{z=0}d\Omega_\alpha &= \iint_{\Omega_\alpha} P_{\text{II}}|_{z=0}d\Omega_\alpha\\
\iint_{\Omega_\alpha} P_{\text{II}}|_{z=h_1}d\Omega_\alpha &= \iint_{\Omega_\alpha} P_{\text{III}}|_{z=h_1}d\Omega_\alpha\\
\iint_{\Omega_\alpha} P_{\text{III}}|_{z=h_1+h_g}d\Omega_\alpha &= \iint_{\Omega_\alpha} P_{\text{IV}}|_{z=h_1+h_g}d\Omega_\alpha\\
\iint_{\Omega_\alpha} P_{\text{IV}}|_{z=h_1+h_g+h_2}d\Omega_\alpha &= \iint_{\Omega_\alpha} P_{\text{V}}|_{z=h_1+h_g+h_2}d\Omega_\alpha
\end{aligned} \tag{9}$$

By subtituting the pressure field in the previous expressions:

$$\begin{aligned}
&\iint_{\Omega_\alpha}\sum_{\mathbf{G}} Z_{\mathbf{G}}\left(\delta_{\mathbf{G}0} + r_{\mathbf{G}}\right)e^{i(\mathbf{K}+\mathbf{G})\mathbf{r}}d\Omega_\alpha = \iint_{\Omega_\alpha} Z\left(A_\alpha^{II} + B_\alpha^{II}\right)d\Omega_\alpha\\
&\iint_{\Omega_\alpha} Z\left(A_\alpha^{II}e^{iq_0h_1} + B_\alpha^{II}e^{-iq_0h_1}\right)d\Omega_\alpha = \sum_{\mathbf{G}} Z_G\left(\tau_{\mathbf{G}} + \Gamma_{\mathbf{G}}\right)e^{i(\mathbf{K}+\mathbf{G})\mathbf{r}}d\Omega_\alpha\\
&\iint_{\Omega_\alpha}\sum_{\mathbf{G}} Z_G\left(\tau_{\mathbf{G}}e^{iq_{\mathbf{G}}h_g} + \Gamma_{\mathbf{G}}e^{-iq_{\mathbf{G}}h_g}\right)e^{i(\mathbf{K}+\mathbf{G})\mathbf{r}}d\Omega_\alpha = \iint_{\Omega_\alpha} Z\left(A_\alpha^{IV} + B_\alpha^{IV}\right)d\Omega_\alpha\\
&\iint_{\Omega_\alpha} Z\left(A_\alpha^{IV}e^{iq_0h_2} + B_\alpha^{IV}e^{-iq_0h_2}\right)d\Omega_\alpha = \iint_{\Omega_\alpha}\sum_{\mathbf{G}} Z_G t_{\mathbf{G}}e^{i(\mathbf{K}+\mathbf{G})\mathbf{r}}d\Omega_\alpha
\end{aligned} \tag{10}$$

After doing the integrals we get:

$$\begin{aligned}
&\sum_{\mathbf{G}} Z_{\mathbf{G}}\left(\delta_{\mathbf{G}0} + r_{\mathbf{G}}\right)H_\alpha^1(\mathbf{G}) = Z\left(A_\alpha^{II} + B_\alpha^{II}\right)\\
&Z\left(A_\alpha^{II}e^{iq_0h_1} + B_\alpha^{II}e^{-iq_0h_1}\right) = \sum_{\mathbf{G}} Z_G\left(\tau_{\mathbf{G}} + \Gamma_{\mathbf{G}}\right)H_\alpha^1(\mathbf{G})\\
&\sum_{\mathbf{G}} Z_G\left(\tau_{\mathbf{G}}e^{iq_{\mathbf{G}}h_g} + \Gamma_{\mathbf{G}}e^{-iq_{\mathbf{G}}h_g}\right)H_\alpha^2(\mathbf{G}) = Z\left(A_\alpha^{IV} + B_\alpha^{IV}\right)\\
&Z\left(A_\alpha^{IV}e^{iq_0h_2} + B_\alpha^{IV}e^{-iq_0h_2}\right) = \sum_{\mathbf{G}} Z_G t_{\mathbf{G}}H_\alpha^2(\mathbf{G})
\end{aligned} \tag{11}$$

- **Normal velocity**: we impose the continuity of the normal velocity through along the entire unit cell.

$$\begin{aligned}
&\iint_{\Omega} v_z^I|_{z=0}e^{-i(\mathbf{K}+\mathbf{G}')\mathbf{r}}d\Omega = \iint_{\Omega} v_z^{II}|_{z=0}e^{-i(\mathbf{K}+\mathbf{G}')\mathbf{r}}d\Omega\\
&\iint_{\Omega} v_z^{II}|_{z=h_1}e^{-i(\mathbf{K}+\mathbf{G}')\mathbf{r}}d\Omega = \iint_{\Omega} v_z^{III}|_{z=h_1}e^{-i(\mathbf{K}+\mathbf{G}')\mathbf{r}}d\Omega\\
&\iint_{\Omega} v_z^{III}|_{z=h_1+h_g}e^{-i(\mathbf{K}+\mathbf{G}')\mathbf{r}}d\Omega = \iint_{\Omega} v_z^{IV}|_{z=h_1+h_g}e^{-i(\mathbf{K}+\mathbf{G}')\mathbf{r}}d\Omega\\
&\iint_{\Omega} v_z^{IV}|_{z=h_1+h_g+h_2}e^{-i(\mathbf{K}+\mathbf{G}')\mathbf{r}}d\Omega = \iint_{\Omega} v_z^{V}|_{z=h_1+h_g+h_2}e^{-i(\mathbf{K}+\mathbf{G}')\mathbf{r}}d\Omega
\end{aligned} \tag{12}$$

By subtituting the normal velocity field in the previous expressions:

$$\begin{aligned}
&\iint_{\Omega}\sum_{\mathbf{G}}(\delta_{\mathbf{G}0} - r_{\mathbf{G}})e^{i(\mathbf{K}+\mathbf{G})\mathbf{r}}e^{-i(\mathbf{K}+\mathbf{G}')\mathbf{r}}d\Omega = \sum_\alpha\iint_{\Omega_\alpha}\left(A_\alpha^{II} - B_\alpha^{II}\right)e^{-i(\mathbf{K}+\mathbf{G}')\mathbf{r}}d\Omega_\alpha\\
&\sum_\alpha\iint_{\Omega_\alpha}\left(A_\alpha^{II}e^{iq_0h_1} - B_\alpha^{II}e^{-iq_0h_1}\right)e^{-i(\mathbf{K}+\mathbf{G}')\mathbf{r}}d\Omega_\alpha = \iint_{\Omega}\sum_{\mathbf{G}}\left(\tau_{\mathbf{G}} - \Gamma_{\mathbf{G}}\right)e^{i(\mathbf{K}+\mathbf{G})\mathbf{r}}e^{-i(\mathbf{K}+\mathbf{G}')\mathbf{r}}d\Omega\\
&\iint_{\Omega}\sum_{\mathbf{G}}\left(\tau_{\mathbf{G}}e^{iq_{\mathbf{G}}h_g} - \Gamma_{\mathbf{G}}e^{-iq_{\mathbf{G}}h_g}\right)e^{i(\mathbf{K}+\mathbf{G})\mathbf{r}}e^{-i(\mathbf{K}+\mathbf{G}')\mathbf{r}}d\Omega = \sum_\alpha\iint_{\Omega_\alpha}\left(A_\alpha^{IV} - B_\alpha^{IV}\right)e^{-i(\mathbf{K}+\mathbf{G}')\mathbf{r}}d\Omega_\alpha\\
&\sum_\alpha\iint_{\Omega_\alpha}\left(A_\alpha^{IV}e^{iq_0h_2} - B_\alpha^{IV}e^{-iq_0h_2}\right)e^{-i(\mathbf{K}+\mathbf{G}')\mathbf{r}}d\Omega_\alpha = \iint_{\Omega}\sum_{\mathbf{G}} t_{\mathbf{G}}e^{i(\mathbf{K}+\mathbf{G})\mathbf{r}}e^{-i(\mathbf{K}+\mathbf{G}')\mathbf{r}}d\Omega
\end{aligned} \tag{13}$$

After doing the integrals we get:

$$\begin{aligned}
&\sum_{\mathbf{G}}(\delta_{\mathbf{G}0} - r_{\mathbf{G}}) = \sum_\alpha\left(A_\alpha^{II} - B_\alpha^{II}\right)H_\alpha^{1*}(\mathbf{G})f_\alpha\\
&\sum_\alpha\left(A_\alpha^{II}e^{iq_0h_1} - B_\alpha^{II}e^{-iq_0h_1}\right)H_\alpha^{1*}(\mathbf{G})f_\alpha = \sum_{\mathbf{G}}\left(\tau_{\mathbf{G}} - \Gamma_{\mathbf{G}}\right)\\
&\sum_{\mathbf{G}}\left(\tau_{\mathbf{G}}e^{iq_{\mathbf{G}}h_g} - \Gamma_{\mathbf{G}}e^{-iq_{\mathbf{G}}h_g}\right) = \sum_\alpha\left(A_\alpha^{IV} - B_\alpha^{IV}\right)H_\alpha^{2*}(\mathbf{G})f_\alpha\\
&\sum_\alpha\left(A_\alpha^{IV}e^{iq_0h_2} - B_\alpha^{IV}e^{-iq_0h_2}\right)H_\alpha^{2*}(\mathbf{G})f_\alpha = \sum_{\mathbf{G}} t_{\mathbf{G}}
\end{aligned} \tag{14}$$

After applying the mode matching technique through the pressure and the normal velocity field, we obtained a system of 8 equations and 8 unknowns wich are: $r_{\mathbf{G}}, \tau_{\mathbf{G}}, \Gamma_{\mathbf{G}}, t_{\mathbf{G}}, A_\alpha^{II}, B_\alpha^{II}, A_\alpha^{IV}$ and B_α^{IV}. In order to solve the system, we are going to first eliminate four of these unknowns by reducing the system from 8 to 4 equations. For doing that, we will combine the result of applying the mode matching through the normal velocity of one region, with the result of applying the method to the pressure field as we can see in the following equations:

$$\begin{aligned}
&\sum_{\mathbf{G}} Z_{\mathbf{G}}\left(\delta_{\mathbf{G}0} + r_{\mathbf{G}}\right)H_\alpha^1(\mathbf{G}) = Z\left(A_\alpha^{II} + B_\alpha^{II}\right)\\
&\left(\delta_{\mathbf{G}0} - r_{\mathbf{G}}\right) = \sum_\alpha\left(A_\alpha^{II} - B_\alpha^{II}\right)H_\alpha^{1*}(\mathbf{G})f_\alpha
\end{aligned} \tag{15}$$

$$Z\left(A_\alpha^{II}e^{iq_0h_1}+B_\alpha^{II}e^{-iq_0h_1}\right)=\sum_{\mathbf{G}}Z_G\left(\tau_{\mathbf{G}}+\Gamma_{\mathbf{G}}\right)H_\alpha^1(\mathbf{G})$$
$$\sum_\alpha\left(A_\alpha^{II}e^{iq_0h_1}-B_\alpha^{II}e^{iq_0h_1}\right)H_\alpha^{1*}(\mathbf{G})f_\alpha=\sum_{\mathbf{G}}\left(\tau_{\mathbf{G}}-\Gamma_{\mathbf{G}}\right) \quad (16)$$

$$\sum_{\mathbf{G}}Z_G\left(\tau_{\mathbf{G}}e^{iq_{\mathbf{G}}h_g}+\Gamma_{\mathbf{G}}e^{-iq_{\mathbf{G}}h_g}\right)H_\alpha^2(\mathbf{G})=Z\left(A_\alpha^{IV}+B_\alpha^{IV}\right)$$
$$\left(\tau_{\mathbf{G}}e^{iq_{\mathbf{G}}h_g}-\Gamma_{\mathbf{G}}e^{-iq_{\mathbf{G}}h_g}\right)=\sum_\alpha\left(A_\alpha^{IV}-B_\alpha^{IV}\right)H_\alpha^{2*}(\mathbf{G})f_\alpha \quad (17)$$

$$Z\left(A_\alpha^{IV}e^{iq_0h_2}+B_\alpha^{IV}e^{-iq_0h_2}\right)=\sum_{\mathbf{G}}Z_G^Vt_{\mathbf{G}}H_\alpha^2(\mathbf{G})$$
$$\sum_\alpha\left(A_\alpha^{IV}e^{iq_0h_2}-B_\alpha^{IV}e^{-iq_0h_2}\right)H_\alpha^{2*}(\mathbf{G})f_\alpha=\sum_{\mathbf{G}}t_{\mathbf{G}}. \quad (18)$$

In order to reduce the system to four equations, we first eliminate $r_{\mathbf{G}}$ in (15), afterwards $\tau_{\mathbf{G}}$ and $\Gamma_{\mathbf{G}}$ in Eq. (16) and (17) and finally, $t_{\mathbf{G}}$ in Eq. (18). We then express the resulting system of equations in terms of the modal velocities:

$$\begin{aligned}v_{1\alpha}&=A_\alpha^{II}-B_\alpha^{II}\\ v'_{1\alpha}&=-\left(A_\alpha^{II}e^{iq_0h_1}-B_\alpha^{II}e^{-iq_0h_1}\right)\\ v_{2\alpha}&=A_\alpha^{IV}-B_\alpha^{IV}\\ v'_{2\alpha}&=-\left(A_\alpha^{IV}e^{iq_0h_2}-B_\alpha^{IV}e^{-iq_0h_2}\right)\end{aligned} \quad (19)$$

First equation

$$r_{\mathbf{G}}=\delta_{\mathbf{G}0}-\sum_\beta\left(A_\beta^{II}-B_\beta^{II}\right)H_\beta^{1*}(\mathbf{G})f_\beta$$

$$Z^{II}\left(A_\alpha^{II}+B_\alpha^{II}\right)+\sum_{\mathbf{G}}Z_{\mathbf{G}}\sum_\beta\left(A_\beta^{II}-B_\beta^{II}\right)H_\beta^{1*}(\mathbf{G})f_\beta H_\alpha^1(\mathbf{G})=\sum_{\mathbf{G}}Z_{\mathbf{G}}2\delta_{\mathbf{G}0}H_\alpha^1(\mathbf{G})$$

$$Z^{II}\left(-\frac{v'_{1\alpha}}{i\sin(q_0h_1)}-\frac{v_{1\alpha}}{i\tan(q_0h_1)}\right)+\sum_\beta M_{\alpha\beta}^Iv_{1\beta}=\sum_{\mathbf{G}}Z_{\mathbf{G}}^I2\delta_{\mathbf{G}0}H_\alpha^1(\mathbf{G})$$

$$\boxed{\left(G_1^{\alpha\alpha}-\epsilon_1\right)v_{1\alpha}+\sum_{\beta\neq\alpha}G_1^{\alpha\beta}v_{1\beta}-G_1^Vv'_{1\alpha}=I^\alpha} \quad (20)$$

Fourth Equation

$$t_{\mathbf{G}}=\sum_\beta\left(A_\beta^{IV}e^{iq_0h_2}-B_\beta^{IV}e^{-iq_0h_2}\right)H_\beta^{2*}(\mathbf{G})f_\beta$$

$$Z^{IV}\left(-\frac{v_{2\alpha}}{i\sin(q_0h_2)}-\frac{v'_{2\alpha}}{i\tan(q_0h_2)2}\right)+\sum_\beta M_{\alpha\beta}^Vv'_{2\beta}=0$$

$$\boxed{\left(G_2^{\alpha\alpha}-\epsilon_2\right)v'_{2\alpha}+\sum_{\beta\neq\alpha}G_2^{\alpha\beta}v'_{2\beta}-G_2^Vv_{2\alpha}=0} \quad (21)$$

Second equation

Eliminating $\Gamma_{\mathbf{G}}$ from Eq. (16)

$$\Gamma_{\mathbf{G}}=\tau_{\mathbf{G}}-\sum_\beta\left(A_\beta^{II}e^{iq_0h_1}-B_\beta^{II}e^{-iq_0h_1}\right)H_\beta^{1*}(\mathbf{G})f_\beta$$

$$Z\left(A_\alpha^{II}e^{iq_0h_1}+B_\alpha^{II}e^{-iq_0h_1}\right)+\sum_\beta M_{\alpha\beta}\left(A_\beta^{II}e^{iq_0h_1}-B_\beta^{II}e^{-iq_0h_1}\right)=\sum_{\mathbf{G}}Z_G2\tau_{\mathbf{G}}H_\alpha^1(\mathbf{G})$$

$$-\frac{Z}{i\sin(q_0h_1)}v_{1\alpha}-\frac{Z}{i\tan(q_0h_1)}v'_{1\alpha}-\sum_\beta M_{\alpha\beta}v'_{1\beta}=\sum_{\mathbf{G}}Z_G2\tau_{\mathbf{G}}H_\alpha^1(\mathbf{G}) \quad (22)$$

Eliminating $\tau_{\mathbf{G}}$ from Eq. (16)

$$\tau_{\mathbf{G}}=\Gamma_{\mathbf{G}}+\sum_\beta\left(A_\beta^{II}e^{iq_0h_1}-B_\beta^{II}e^{-iq_0h_1}\right)H_\beta^{1*}(\mathbf{G})f_\beta$$

$$Z\left(A_\alpha^{II}e^{iq_0h_1}+B_\alpha^{II}e^{-iq_0h_1}\right)-\sum_\beta M_{\alpha\beta}\left(A_\beta^{II}e^{iq_0h_1}-B_\beta^{II}e^{-iq_0h_1}\right)=\sum_{\mathbf{G}}Z_G2\Gamma_{\mathbf{G}}H_\alpha^1(\mathbf{G})$$

$$-\frac{Z}{i\sin(q_0h_1)}v_{1\alpha}-\frac{Z}{i\tan(q_0h_1)}v'_{1\alpha}+\sum_\beta M_{\alpha\beta}v'_{1\beta}=\sum_{\mathbf{G}}Z_G2\Gamma_{\mathbf{G}}H_\alpha^1(\mathbf{G}) \quad (23)$$

By doing (22)$e^{iq_{\mathbf{G}}^{III}h_g}$ - (23)$e^{-iq_{\mathbf{G}}^{III}h_g}$ we get:

$$\begin{aligned}-\frac{Z}{i\sin(q_0h_1)}v_{1\alpha}\left(e^{iq_{\mathbf{G}}h_g}-e^{-iq_{\mathbf{G}}h_g}\right)-\frac{Z}{i\tan(q_0h_1)}v'_{1\alpha}\left(e^{iq_{\mathbf{G}}h_g}-e^{-iq_{\mathbf{G}}h_g}\right)\\ -\sum_\beta M_{\alpha\beta}v'_{1\beta}\left(e^{iq_{\mathbf{G}}h_g}+e^{-iq_{\mathbf{G}}h_g}\right)\\ =\sum_{\mathbf{G}}Z_G2H_\alpha^1(\mathbf{G})\left(\tau_{\mathbf{G}}e^{iq_{\mathbf{G}}h_g}-\Gamma_{\mathbf{G}}e^{-iq_{\mathbf{G}}h_g}\right)\end{aligned}$$

We divide the whole equation by $e^{iq_{\mathbf{G}}^{III}h_g}-e^{-iq_{\mathbf{G}}^{III}h_g}$

$$\begin{aligned}-\frac{Z}{i\sin(q_0h_1)}v_{1\alpha}-\frac{Z}{i\tan(q_0h_1)}v'_{1\alpha}-\sum_\beta M_{\alpha\beta}v'_{1\beta}\frac{\left(e^{iq_{\mathbf{G}}h_g}+e^{-iq_{\mathbf{G}}h_g}\right)}{\left(e^{iq_{\mathbf{G}}^{III}h_g}-e^{-iq_{\mathbf{G}}h_g}\right)}\\ -\frac{\sum_\beta 2M_{\alpha\beta}}{\left(e^{iq_{\mathbf{G}}h_g}-e^{-iq_{\mathbf{G}}h_g}\right)}v_{2\beta}=0\end{aligned}$$

$$\frac{Z^{II}}{i\sin(q_0h_1)}v_{1\alpha}+\frac{Z}{i\tan(q_0h_1)}v'_{1\alpha}+\sum_\alpha M_{\alpha\beta}v'_{1\beta}\frac{\cos(q_{\mathbf{G}}h_g)}{i\sin(q_{\mathbf{G}}h_g)}+\sum_\beta\frac{M_{\alpha\beta}}{i\sin(q_{\mathbf{G}}h_g)}v_{2\beta}=0$$

$$\left(\frac{M_{\alpha\alpha}}{i\tan(q_{\mathbf{G}}h_g)}+\frac{Z}{i\tan(q_0h_1)}\right)v'_{1\alpha}+\sum_{\beta\neq\alpha}\frac{M_{\alpha\beta}}{i\tan(q_{\mathbf{G}}h_g)}v'_{1\beta}+\sum_\beta\frac{M_{\alpha\beta}}{i\sin(q_{\mathbf{G}}h_g)}v_{2\beta}+\frac{Z}{i\sin(q_0h_1)}v_{1\alpha}=0$$

$$\boxed{\left(\psi_{\alpha\alpha}^1+\epsilon_1\right)v'_{1\alpha}+\sum_{\beta\neq\alpha}\psi_{\alpha\beta}^1v'_{1\beta}+\sum_\beta\Phi_{\alpha\beta}v_{2\beta}+G_1^Vv_{1\alpha}=0} \quad (24)$$

Third equation

Eliminating $\tau_{\mathbf{G}}e^{iq_{\mathbf{G}}^{III}h_g}$ from Eq. (17):

$$Z\left(A_\alpha^{IV}+B_\alpha^{IV}\right)-\sum_\beta M_{\alpha\beta}\left(A_\beta^{IV}-B_\beta^{IV}\right)=\sum_{\mathbf{G}}Z_G2\Gamma_{\mathbf{G}}e^{-iq_{\mathbf{G}}h_g}H_\alpha^2(\mathbf{G})$$

$$-\frac{Z}{i\sin(q_0h_2)}v'_{2\alpha}-\frac{Z}{i\tan(q_0h_2)}v_{2\alpha}-\sum_\beta M_{\alpha\beta}v_{2\beta}=\sum_{\mathbf{G}}Z_G2\Gamma_{\mathbf{G}}e^{-iq_{\mathbf{G}}h_g}H_\alpha^2(\mathbf{G}) \quad (25)$$

Eliminating $\Gamma_{\mathbf{G}}e^{-iq_{\mathbf{G}}h_g}$ fromEq. (17):

$$Z\left(A_\alpha^{IV}+B_\alpha^{IV}\right)+\sum_\beta M_{\alpha\beta}\left(A_\beta^{IV}-B_\beta^{IV}\right)=\sum_{\mathbf{G}}Z_G2\tau_{\mathbf{G}}e^{iq_{\mathbf{G}}h_g}H_\alpha^2(\mathbf{G})$$

$$-\frac{Z}{i\sin(q_0h_2)}v'_{2\alpha}-\frac{Z}{i\tan(q_0h_2)}v_{2\alpha}+\sum_\beta M_{\alpha\beta}v_{2\beta}=\sum_{\mathbf{G}}Z_G2\tau_{\mathbf{G}}e^{iq_{\mathbf{G}}h_g}H_\alpha^2(\mathbf{G}) \quad (26)$$

By doing -(25)$e^{iq_{\mathbf{G}}^{III}h_g}$ + (26)$e^{-iq_{\mathbf{G}}^{III}h_g}$ we get:

$$\begin{aligned}\frac{Z}{i\sin(q_0h_2)}v'_{2\alpha}\left(e^{iq_{\mathbf{G}}h_g}-e^{-iq_{\mathbf{G}}h_g}\right)+\frac{Z}{i\tan(q_0h_2)}v_{2\alpha}\left(e^{iq_{\mathbf{G}}h_g}-e^{-iq_{\mathbf{G}}h_g}\right)\\ +\sum_\beta M_{\alpha\beta}v_{2\beta}\left(e^{iq_{\mathbf{G}}h_g}-e^{-iq_{\mathbf{G}}h_g}\right)\\ =\sum_{\mathbf{G}}Z_G2H_\alpha^2(\mathbf{G})\left(\tau_{\mathbf{G}}-\Gamma_{\mathbf{G}}\right)\end{aligned}$$

We divide the whole equation by $e^{iq_{\mathbf{G}}^{III}h_g}-e^{-iq_{\mathbf{G}}^{III}h_g}$

$$\begin{aligned}\frac{Z}{i\sin(q_0h_2)}v'_{2\alpha}+\frac{Z}{i\tan(q_0h_2)}v_{2\alpha}+\sum_\beta M_{\alpha\beta}v_{2\beta}\frac{\left(e^{iq_{\mathbf{G}}h_g}-e^{-iq_{\mathbf{G}}h_g}\right)}{\left(e^{iq_{\mathbf{G}}h_g}-e^{-iq_{\mathbf{G}}h_g}\right)}\\ +\sum_\beta\frac{2M_{\alpha\beta}}{\left(e^{iq_{\mathbf{G}}h_g}-e^{-iq_{\mathbf{G}}h_g}\right)}v'_{1\beta}=0\end{aligned}$$

$$\begin{aligned}\frac{Z}{i\sin(q_0h_2)}v'_{2\alpha}+\frac{Z}{i\tan(q_0h_2)}v_{2\alpha}+\sum_\beta M_{\alpha\beta}v_{2\beta}\frac{2\cos(q_{\mathbf{G}}h_g)}{2i\sin(q_{\mathbf{G}}h_g)}\\ -\sum_\beta\frac{2M_{\alpha\beta}}{2i\sin(q_{\mathbf{G}}h_g)}v'_{1\beta}=0\end{aligned}$$

$$\begin{aligned}\left(\frac{M_{\alpha\alpha}}{i\tan(q_{\mathbf{G}}h_g)}+\frac{Z}{i\tan(q_0h_2)}\right)v_{2\alpha}+\sum_{\beta\neq\alpha}\frac{M_{\alpha\beta}}{i\tan(q_{\mathbf{G}}h_g)}v_{2\beta}\\ +\sum_\beta\frac{M_{\alpha\beta}}{i\sin(q_{\mathbf{G}}h_g)}v'_{1\beta}+\frac{Z}{i\sin(q_0h_2)}v'_{2\alpha}=0\end{aligned}$$

$$\boxed{\left(\psi_{\alpha\alpha}+\epsilon_2\right)v_{2\alpha}+\sum_{\beta\neq\alpha}\psi_{\alpha\beta}v_{2\beta}+\sum_\beta\Phi_{\alpha\beta}v'_{1\beta}+G_2^Vv'_{2\alpha}=0} \quad (27)$$

Final system of equations As this is a linear system of equations, we can express it in matrix formulation. Thus, the modal velocities can be easily solved by means of the following expression:

$$\boxed{\begin{aligned}\left(G_1^{\alpha\alpha}-\epsilon_1\right)v_{1\alpha}+\sum_{\beta\neq\alpha}G_1^{\alpha\beta}v_{1\beta}-G_1^Vv'_{1\alpha}&=I^\alpha\\ \left(\psi_{\alpha\alpha}^1+\epsilon_1\right)v'_{1\alpha}+\sum_{\beta\neq\alpha}\psi_{\alpha\beta}^1v'_{1\beta}+\sum_\beta\Phi_{\alpha\beta}^1v_{2\beta}+G_1^Vv_{1\alpha}&=0\\ \left(\psi_{\alpha\alpha}^2+\epsilon_2\right)v_{2\alpha}+\sum_{\beta\neq\alpha}\psi_{\alpha\beta}^2v_{2\beta}+\sum_\beta\Phi_{\alpha\beta}^2v'_{1\beta}+G_2^Vv'_{2\alpha}&=0\\ \left(G_2^{\alpha\alpha}-\epsilon_2\right)v'_{2\alpha}+\sum_{\beta\neq\alpha}G_2^{\alpha\beta}v'_{2\beta}-G_2^Vv_{2\alpha}&=0\end{aligned}} \quad (28)$$

with:

$$
\begin{aligned}
M_{\alpha\beta} &= \sum_{\mathbf{G}} Z_{\mathbf{G}} H^{*}_{\beta}(\mathbf{G}) f_{\beta} H_{\alpha}(\mathbf{G}) \\
I^{\alpha} &= \sum_{\mathbf{G}} 2 Z_{\mathbf{G}} \delta_{\mathbf{G}0} H^{1}_{\alpha}(\mathbf{G}) \\
H^{1(2)}_{\alpha}(\mathbf{G}) &= \frac{2J_1(R_{0\alpha}|\mathbf{K}+\mathbf{G}|)}{R_{0\alpha}|\mathbf{K}+\mathbf{G}|} e^{i(\mathbf{K}+\mathbf{G})\mathbf{R}^{1(2)}_{\alpha}} \\
G^{V}_{1} &= \frac{Z}{i\sin(q_0 h_1)} \\
G^{V}_{2} &= \frac{Z}{i\sin(q_0 h_2)} \\
\epsilon_1 &= \frac{Z}{i\tan(q_0 h_1)} \\
\epsilon_2 &= \frac{Z}{i\tan(q_0 h_2)} \\
G^{1(2)}_{\alpha\beta} &= \sum_{\mathbf{G}} Z_{\mathbf{G}} H^{*1(2)}_{\beta}(\mathbf{G}) f_{\beta} H^{1(2)}_{\alpha}(\mathbf{G}) \\
\psi^{1(2)}_{\alpha\beta} &= \sum_{\mathbf{G}} \frac{Z_{\mathbf{G}} H^{*1(2)}_{\beta}(\mathbf{G}) f_{\beta} H^{1(2)}_{\alpha}(\mathbf{G})}{i\tan(q^{III}_{\mathbf{G}} h_g)} \\
\Phi^{1(2)}_{\alpha\beta} &= \sum_{\mathbf{G}} \frac{Z_{\mathbf{G}} H^{*1(2)}_{\beta}(\mathbf{G}) f_{\beta} H^{1(2)}_{\alpha}(\mathbf{G})}{i\sin(q_{\mathbf{G}} h_g)} \\
f_{\beta} &= \frac{\Omega_{\beta}}{\Omega} = \frac{\pi R^2_{0\beta}}{\sqrt{3}a^2/2}
\end{aligned}
\tag{29}
$$

Data availability

The data that support the findings of this study are available from the corresponding author on reasonable request.

Code availability

The code for obtaining the results of this work are available from the corresponding author upon reasonable request.

Received: 26 March 2022; Accepted: 11 November 2022;
Published online: 15 December 2022

References

1. Lopes dos Santos, J. M. B., Peres, N. M. R. & Castro Neto, A. H. Graphene bilayer with a twist: electronic structure. *Phys. Rev. Lett.* **99**, 256802 (2007).
2. Suárez Morell, E., Correa, J. D., Vargas, P., Pacheco, M. & Barticevic, Z. Flat bands in slightly twisted bilayer graphene: tight-binding calculations. *Phys. Rev. B* **82**, 121407 (2010).
3. Bistritzer, R. & MacDonald, A. H. Moiré bands in twisted double-layer graphene. *Proc. Natl Acad. Sci. USA* **108**, 12233–12237 (2011).
4. Lopes dos Santos, J. M. B., Peres, N. M. R. & Castro Neto, A. H. Continuum model of the twisted graphene bilayer. *Phys. Rev. B* **86**, 155449 (2012).
5. San-Jose, P., González, J. & Guinea, F. Non-abelian gauge potentials in graphene bilayers. *Phys. Rev. Lett.* **108**, 216802 (2012).
6. Cao, Y. et al. Unconventional superconductivity in magic-angle graphene superlattices. *Nature* **556**, 43–50 (2018).
7. Wang, P., Lu, L. & Bertoldi, K. Topological phononic crystals with one-way elastic edge waves. *Phys. Rev. Lett.* **115**, 104302 (2015).
8. He, C. et al. Acoustic topological insulator and robust one-way sound transport. *Nat. Phys.* **12**, 1124–1129 (2016).
9. Zhang, X., Xiao, M.-M., Cheng, Y., Lu, M.-H. & Christensen, J. Topological sound. *Commun. Phys.* **1**, 97 (2018).
10. Ni, X., Weiner, M., Alu, A. & Khanikaev, A. B. Observation of higher-order topological acoustic states protected by generalized chiral symmetry. *Nat. Mater.* **18**, 113–120 (2019).
11. Zhang, X. et al. Dimensional hierarchy of higher-order topology in three-dimensional sonic crystals. *Nat. Commun.* **10**, 5331 (2019).
12. Xue, H. et al. Realization of an acoustic third-order topological insulator. *Phys. Rev. Lett.* **122**, 244301 (2019).
13. Zhang, Z. et al. Deep-subwavelength holey acoustic second-order topological insulators. *Adv. Mater.* **31**, 1904682 (2019).
14. Ni, X., Li, M., Weiner, M., Alù, A. & Khanikaev, A. B. Demonstration of a quantized acoustic octupole topological insulator. *Nat. Commun.* **11**, 2108 (2020).
15. Zheng, L.-Y. & Christensen, J. Dirac hierarchy in acoustic topological insulators. *Phys. Rev. Lett.* **127**, 156401 (2021).
16. Wu, X. et al. Topological corner modes induced by dirac vortices in arbitrary geometry. *Phys. Rev. Lett.* **126**, 226802 (2021).
17. Dorrell, W., Pirie, H., Gardezi, S. M., Drucker, N. C. & Hoffman, J. E. van der waals metamaterials. *Phys. Rev. B* **101**, 121103 (2020).
18. Rosendo López, M., Peñaranda, F., Christensen, J. & San-Jose, P. Flat bands in magic-angle vibrating plates. *Phys. Rev. Lett.* **125**, 214301 (2020).
19. Deng, Y. et al. Magic-angle bilayer phononic graphene. *Phys. Rev. B* **102**, 180304 (2020).
20. Martí-Sabaté, M. & Torrent, D. Dipolar localization of waves in twisted phononic crystal plates. *Phys. Rev. Appl.***15**, L011001 (2021).
21. Gardezi, S. M., Pirie, H., Carr, S., Dorrell, W. & Hoffman, J. E. Simulating twistronics in acoustic metamaterials. *2D Mater.* **8**, 031002 (2021).
22. Oudich, M. et al. Photonic analog of bilayer graphene. *Phys. Rev. B* **103**, 214311 (2021).
23. Christensen, J., Martin-Moreno, L. & Garcia-Vidal, F. J. Theory of resonant acoustic transmission through subwavelength apertures. *Phys. Rev. Lett.* **101**, 014301 (2008).
24. Torrent, D. Acoustic anomalous reflectors based on diffraction grating engineering. *Phys. Rev. B* **98**, 060101 (2018).

Acknowledgements

J.C. acknowledges the support from the European Research Council (ERC) through the Starting Grant 714577 PHONOMETA. Z.Z. acknowledges the support from the NSFC (12104226), the China National Postdoctoral Program for Innovative Talents (BX20200165) and the China Postdoctoral Science Foundation (2020M681541). D.T. acknowledges the support of MINECO through a Ramón y Cajal grant (Grant No. RYC-2016-21188) and of the Ministry of Science, Innovation and Universities trough project number RTI2018-093921-A-C42. J.C. is grateful to stimulating discussions with Pablo San-Jose and Niels Gregersen.

Author contributions

J.C. and Z. Z. conceived the project. M.R.-L., D.T., and J. C. developed the theory. M.R.-L. and Z.Z. conducted all simulations.

Competing interests

The authors declare no competing interests. Johan Christensen is a Guest Editor for Communications Materials and was not involved in the editorial review of, or the decision to publish, this Article.

Additional information

Correspondence and requests for materials should be addressed to Zhiwang Zhang or Johan Christensen.

Peer review information *Communications Materials* thanks Nikhil JRK Gerard, Alexander Khanikaev and the other, anonymous, reviewer(s) for their contribution to the peer review of this work. Primary Handling Editor: Aldo Isidori.

Reprints and permission information is available at http://www.nature.com/reprints

Publisher's note Springer Nature remains neutral with regard to jurisdictional claims in published maps and institutional affiliations.